

# Origin of yield stress and mechanical plasticity in biological tissues

Anh Q Nguyen, Junxiang Huang, and Dapeng Bi

*Department of Physics, Northeastern University, Boston, MA 02115, USA and  
Center for Theoretical Biological Physics, Northeastern University, Boston, Massachusetts 02215, USA*

During development and under normal physiological conditions, biological tissues are continuously subjected to substantial mechanical stresses. In response to large deformations cells in a tissue must undergo multicellular rearrangements in order to maintain integrity and robustness. However, how these events are connected in time and space remains unknown. Here, using computational and theoretical modeling, we studied the mechanical plasticity of epithelial monolayers under large deformations. Our results demonstrate that the jamming-unjamming (solid-fluid) transition in tissues can vary significantly depending on the degree of deformation, implying that tissues are highly unconventional materials. Using analytical modeling, we elucidate the origins of this behavior. We also demonstrate how a tissue accommodates large deformations through a collective series of rearrangements, which behave similarly to avalanches in non-living materials. We find that these ‘tissue avalanches’ are governed by stress redistribution and the spatial distribution of vulnerable spots. Finally, we propose a simple and experimentally accessible framework to predict avalanches and infer tissue mechanical stress based on static images.

## I. INTRODUCTION

During morphogenesis and under normal physiological conditions, biological tissues continuously experience substantial mechanical stresses [1]. Research efforts to understand the remarkable deformability of epithelial tissues employ both experimental and simulation approaches. Experimentally, studies focus on the tissue’s responses to external stresses [2–5], where a stress-driven unjamming transition has been noted [4]. On the simulation front, the cellular Potts and Vertex-based models are utilized to probe tissue rheology [6, 7], uncovering nonlinear elasticity and rheological properties [7, 8]. However, with few exceptions [9], research has predominantly focused on the shear startup regime. This leaves a gap in our understanding of tissue behavior under steady shear and the mechanisms underpinning yield-stress behavior in tissues. Beyond the yield stress, materials typically flow through plastic rearrangements. Similarly, within tissues, mechanical plasticity occurs through cellular rearrangements, enabling the maintenance of integrity and robustness. While there is extensive literature on how individual cells rearrange with their neighbors [10–13], significant gaps remain in understanding how these localized events connect over time and space. Moreover, a major challenge lies in elucidating how these collective interactions lead to mechanical responses at the tissue level. In the context of material plasticity, avalanche-like behavior, prevalent in phenomena ranging from earthquakes to ferromagnets, involves small perturbations triggering significant collective responses [14]. Systems exhibiting these instabilities display self-organized criticality [15] and power law scaling in their observables, indicating the universality class of the process. Proliferation-driven avalanche-like behavior has recently been observed in the *Drosophila* eye disc, suggesting that avalanches provide a macroscopic mechanism for epithelial tissues to alleviate accumulated proliferative stress [16]. Moreover, shear-induced avalanches have been documented in vertex-based models [8, 9, 17], yet a detailed examination of these avalanches’ growth is still lacking.

In this work, we investigate tissue mechanical plastic-

ity using the Voronoi-based Vertex model under quasi-static shear. Our results demonstrate that the solid-fluid transition point—also referred to as the jamming-unjamming transition in recent literature—does not occur at a singular point but varies depending on the degree of shear deformation the tissue undergoes. Furthermore, challenging traditional definitions, we discover states where tissues possess yield-stress properties but lack a conventional shear modulus. These states exist in a solid-fluid coexistence phase near the jamming-unjamming transition, which we explore through a modified version of the Soft Glassy Rheology (SGR) model to elucidate the origins of these complex states. Our research not only clarifies how tissue manages large deformations through multicellular rearrangements akin to avalanches observed in non-living materials but also connects these phenomena to the tissue-level mechanical responses discussed earlier. These “tissue avalanches” are driven by stress redistribution and the spatial distribution of vulnerable spots, elements that echo the earlier discussions on mechanical responses and rheological properties. By quantifying the spatial and temporal correlations within these rearrangements, we advance the field’s understanding and propose a novel methodological framework capable of predicting collective rearrangements and inferring tissue stress from static snapshots of tissue configuration.

## II. RESULTS

### A. The confluent jamming transition is not unique

To investigate the mechanical behavior of dense epithelial tissues under substantial deformation, we employed a Voronoi-based Vertex model [8, 18]. The cell centers  $\{\mathbf{r}_i\}$  and their geometric configurations are derived from Voronoi tessellation. The biomechanical interactions are captured through a dimensionless mechanical energy functional [19] expressed as:

$$\varepsilon = \sum_{i=1}^N [\kappa_A (a_i - 1)^2 + (p_i - p_0)^2], \quad (1)$$

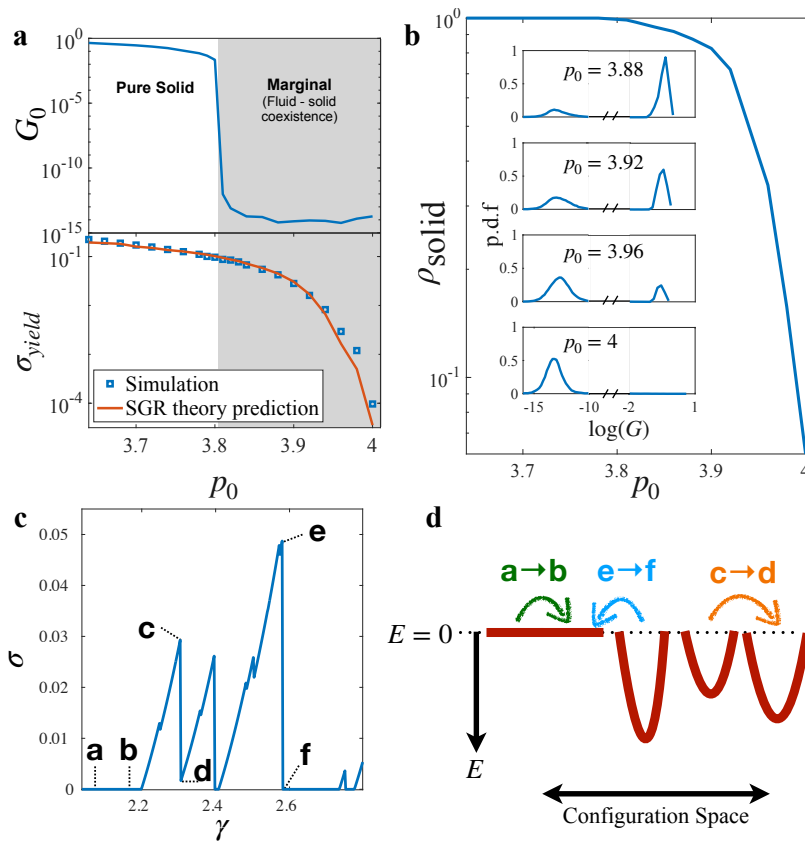


FIG. 1. (a) Discrepancy between shear start-up and steady-shear regime. Top: The shear modulus of the un-sheared tissue ( $\gamma = 0$ ). The shear modulus is obtained using linear-response calculation (see Methods). Bottom: The yield stress  $\sigma_{yield}$  obtained from the steady-state shear regime of quasistatic simulations is shown together with the yield stress obtained from the SGR model, where the only fitting parameter in the model, the elastic constant of an element was chosen to be  $k = 0.0386$ . (b) The probability of finding the system in solid state as a function of  $p_0$ . Inset: Distribution of tissue stress at different  $p_0$ . (c) Stress-strain curve example showing different yielding types: a fluid state yields to another fluid states  $a \rightarrow b$ , a solid state yields to another solid one  $c \rightarrow d$ , and a solid state yields to a fluid state  $e \rightarrow f$ . (d) Schematic of the dynamics of elements in the SGR model: The energy landscape of the material consists of traps with different depth  $E$  drawn from a distribution  $\rho(E)$  that characterizes the structural disorder of the material. Yielding events are captured by transitions from one trap to another. The three types of transition illustrates the transitions observed in simulation

where  $a_i$  and  $p_i$  are the dimensionless area and perimeter of each cell,  $\kappa_A$  is the rescaled area elasticity, and  $p_0$  is the preferred cell shape index (see Methods). To probe tissue response, we applied quasi-static simple-shear deformation using Lees-Edwards boundary conditions, incrementally increasing strain with the FIRE algorithm to minimize energy (see Methods).

In the unsheared version of the vertex model, it has been demonstrated that the preferred cell shape index  $p_0$  drives a rigidity transition at  $p_0 = p_0^* \approx 3.81$ , where the linear response shear modulus vanishes [20]. Recent studies have shown that beyond this transition point, in the liquid phase ( $p_0 > p_0^*$ ), the model can undergo strain-stiffening, indicating a rigidity gain upon strain application. In our quasi-static shearing protocol, we explore beyond the linear response and shear startup regimes into the large deformation limit. In this regime, the tissue exhibits plastic flow primarily through cell-cell rearrangements, or T1 transitions. Here the mean shear stress corresponds to the tissue's yield stress

$$\sigma_{yield} = \lim_{\dot{\gamma} \rightarrow 0} \langle \sigma_{xy}(\dot{\gamma}) \rangle. \quad (2)$$

As illustrated in Fig.1a, while the startup shear modulus vanishes at the rigidity transition at  $p_0 \approx 3.81$ , signaling a solid-

to-fluid transition, the yield stress  $\sigma_{yield}$  does not disappear. Instead, it vanishes at a higher cell shape index,  $p_0 \approx 4$ . This underscores a drastic difference in tissue responses between the transient shear startup and steady-shear regimes.

Under steady shear and at shape indices higher than the rigidity transition associated with shear startup (i.e., at  $p_0 > p_0^*$ ), initially fluid-like systems can intermittently exhibit solid-like behavior before reverting to fluid-like states after yielding (Fig.1c). In this context, states with finite shear modulus are considered solid-like (e.g., states **c**, **d**, **f** in Fig.1c), while states that do not resist shear deformation, indicated by having zero shear modulus, are fluid-like (e.g., states **a**, **b**, **e** in Fig.1c). This coexistence therefore shows up as a bimodal distribution of the shear modulus,  $p.d.f(G)$  shown in Fig. 1b, where the fluid phase is associated with a peak near the numerical noise floor of shear modulus ( $\sim 10^{-12}$ ) while the solid phase corresponds to a finite shear modulus.

The shifting behavior in the distributions can be quantified by the fraction of solid states  $\rho_{solid}$  shown in Fig.1b. States below the rigidity transition  $p_0 = p_0^* \approx 3.81$  therefore are always in the solid phase, which we term a **pure solid**. In the range of  $p_0 \in [3.81, 4]$ ,  $\rho_{solid}$  drops below 1 indicating a solid-fluid coexistence, which we will refer to as **marginal**.

For  $p_0 > 4$  the tissue remains always in the fluid phase as it cannot build up stresses in response to shear strain. This is also consistent with the yield stress vanishing at  $p_0 \simeq 4.0$ . The fact that the material response depends on the application of shear is reminiscent of shear jamming in granular materials, where an state below the isotropic (un-sheared) jamming threshold can be jammed with the application of shear [21–24]. The coexistence of solid and fluid phases also has analogs in dense suspensions near shear jamming [25] and discontinuous shear thickening [9, 26].

### B. Predicting the tissue yield stress using a refined Soft Glassy Rheology model

Given the continuous behavior of yield stress across the pure solid - marginal state transition, we aimed to develop a unified model to deepen our qualitative and predictive understanding the steady-shear regime properties using the Soft Glassy Rheology (SGR) framework [27, 28]. In the SGR model, mesoscopic elements, characterized by elastic constant  $k$  and local strain  $l$ , are confined within energy traps  $E$ , where they accumulate elastic energy as macroscopic strain increases, approaching a yield point either directly or through an activated "hop" driven by mechanical fluctuations from neighboring elements yielding. The material's dynamics under shear are governed by the probability  $P(E, l, t)$ , which follows the stochastic differential equation [27, 28]:

$$\frac{\partial}{\partial t} P(E, l, t) = -\dot{\gamma} \frac{\partial P}{\partial l} - \Gamma_0 e^{[E - kl^2/2]/x} P + \Gamma(t) \rho(E) \delta(l). \quad (3)$$

Here the first term in Eq. 3 describes the motion of the elements caused by global shear rate  $\dot{\gamma}$ . The second term captures activated hopping from a trap of depth  $E - kl^2/2$  (corresponding to the distance to yielding).  $x$  represents the mechanical noise in the system akin to temperature. The final term illustrates the transition to new states, with  $(E, l = 0)$  following yield, selected from a quenched random distribution  $\rho(E)$ .

In the SGR model, the choice of  $\rho(E)$ 's functional form critically influences material behavior [28]. Direct measurement of energy barrier distributions is challenging, leading prior studies to adopt generic or ad hoc assumptions for  $\rho(E)$ , such as exponential distributions [29–31]. In this work, we introduce a novel approach based on distinct mesoscopic tissue phases observed: (1) fluid elements with zero yielding energy ( $E = 0$ ) and (2) solid elements with finite yielding energy ( $E > 0$ ). Consequently, we propose a refined  $\rho(E)$ :

$$\rho(E) = f_0 \delta(E) + (1 - f_0) \frac{E^{\kappa-1} e^{-E/x_0}}{\Gamma(\kappa) x_0^\kappa}. \quad (4)$$

Here,  $f_0$  denotes the probability of an element transitioning to a state with  $E = 0$ , and  $1 - f_0$  corresponds to transitions into states with energy sampled from a  $k$ -gamma distribution, parameterized by mean  $x_0$  and shape factor  $\kappa$ . This is based on the previous observation that the energy barriers to the T1 transition follow a  $k$ -gamma distribution [20, 32] with  $\kappa \approx 2$ .

Together, Eqs. 3 and 4 describe three potential transitions in the energy landscape, depicted in Fig. 1d: (1) fluid to fluid **a**  $\rightarrow$  **b**, (2) solid to solid **c**  $\rightarrow$  **d**, and (3) solid to fluid **e**  $\rightarrow$  **f**.

We next examine the steady state behavior of Eq. 3 in the quasi-static limit ( $\dot{\gamma} \rightarrow 0$ ), with details shown in the Appendix. The behavior is governed by three parameters: the dimensionless ratio of mechanical noise to mean yielding energy  $\chi = x/x_0$ , the probability  $f_0$  of transitioning to a fluid state, and the elastic constant  $k$  of solid elements.

An important aspect of the SGR model is that the fluctuations that drive element rearrangements come from the mechanical noise due to other surrounding rearrangement events in the system. These fluctuations are analogous to the energies released during yielding events observed in our simulations. To correlate this mechanical noise with our empirical data, we introduce the following relationship:

$$\chi = \frac{x}{x_0} \propto \frac{\langle \Delta E \rangle}{\langle E \rangle}. \quad (5)$$

Here,  $\langle \Delta E \rangle$  represents the average energy dissipated during yielding events, while  $\langle E \rangle$  denotes the average energy of cells in their solid state. Next, by analyzing the steady-state solution of Eq. 3, we determine the probability that an element is in the solid phase as a function of  $f_0$  (details in SI, Eq. S.12). This corresponds precisely to  $\rho_{solid}$  in our simulations (Fig. 1b). Finally, we treat the elastic constant  $k$  of the elements as a constant, independent of the shape index  $p_0$ . Given that both  $\langle \Delta E \rangle / \langle E \rangle$  and  $\rho_{solid}$  depend on  $p_0$ , the yield stress predicted by the SGR model (detailed in the SI) effectively varies only with  $p_0$ . This approach contrasts with previous studies that employed the SGR model [29–31, 33], where  $\chi = x/x_0$  was often used as a fitting parameter. In our research, we derive  $\chi$  directly from simulation data, enhancing the predictive accuracy of our theoretical results and distinguishing our use of the SGR model as predictive rather than merely descriptive. In Fig. 1a, we plot the SGR-predicted yield stress as a function of  $p_0$ . This demonstrates that the SGR model accurately predicts the yield stress vanishing point and its dependence on the cell shape index  $\sigma_{yield}(p_0)$ .

The dual-state SGR model identifies two primary mechanisms responsible for the yield stress transition: **(1)** As  $p_0$  increases, states with zero yielding energy barriers become more prevalent, leading to frequent yielding under deformation. This behavior is depicted by transitions such as **a**  $\rightarrow$  **b** and **e**  $\rightarrow$  **f** in Fig. 1d; **(2)** Concurrently, mechanical noise from stress redistributions approaches the scale of the yielding energy barriers, enhancing the likelihood of solid-solid transitions through activated processes induced by neighboring rearrangements, as illustrated by **c**  $\rightarrow$  **d** and **e**  $\rightarrow$  **f**.

### C. Dynamics of tissue plasticity

So far, we know that for a system in the coexistence phase to transitions from solid to fluid, a collective rearrangement event is required to significantly remodel the configuration.

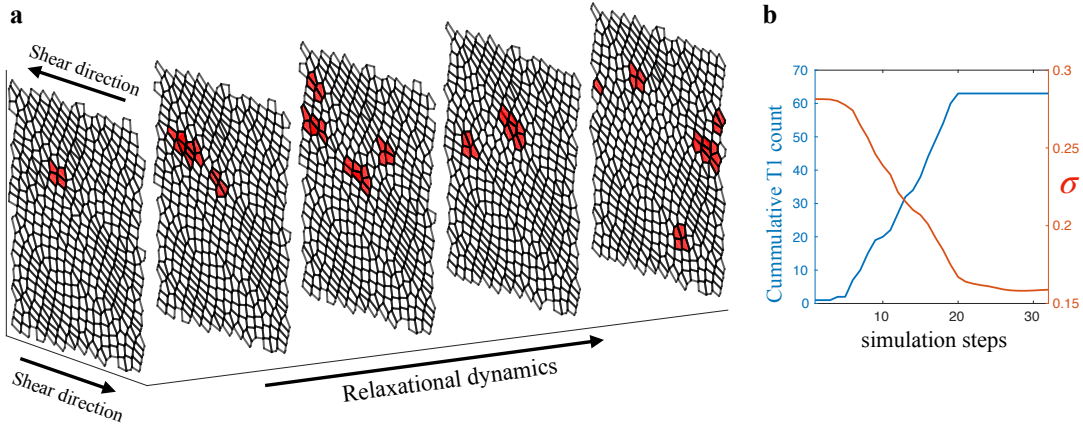


FIG. 2. Spatiotemporal map of plastic events in tissue. **(a)** Space-time map of plastics rearrangement in the form of T1 transition during an avalanche. Cells that participated in T1 transitions are labeled in red. The example avalanche was selected from a system at  $p_0 = 3.72$ . **(b)** Number of accumulative plastic rearrangement and tissue shear stress as the avalanche progresses.

However, the mechanism that govern the occurrences of these events and the evolution of the system during the events is still not fully understood. To explore the yielding behavior of biological tissues, it is essential to describe the dynamics of plastic events during avalanches. In this study, we examine the plasticity dynamics by investigating the spatiotemporal evolution of the plastic rearrangements created by other rearrangements during an avalanche [34, 35]. Fig. 2a displays a space-time plot of the occurrences of T1 transitions during an avalanche, with the cells labeled in red indicating participation in the T1 transitions.

As depicted in Fig. 2a, an avalanche involving numerous plastic rearrangements could originate from a single T1 transition, which we refer to as the initial trigger. Starting from the initial trigger, the stress redistribution from each event can also stimulate surrounding cells to become unstable and undergo T1 transitions. These vulnerable cells have been referred to as soft spots [36, 37] or STZs [38, 39]. This cascade of cellular rearrangements can therefore lead to an avalanche, which continues until the population of soft spots are sufficiently depleted. In Fig. 2b, we show the number of accumulated T1 transitions and the tissue shear stress during a typical avalanche. The stress relaxation due to an avalanche therefore is the origin of the discontinuous yielding of stress during quasistatic shear. In Fig. 2a, the location of rearrangements over time suggests that there is a preferred direction for the avalanche to propagate. In order to quantify this and to establish a causal relationship in time, we define a two-point, two-time correlation function:

$$\phi(\mathbf{r}, \Delta t) = \langle P(\mathbf{r}_0, t_0) P(\mathbf{r}_0 + \mathbf{r}, t_0 + \Delta t) \rangle, \quad (6)$$

where  $P(\mathbf{r}, t)$  is a binary field, representing the occurrence of a T1 transition (1 if a T1 transition occurs at  $\mathbf{r}$  and time  $t$  and 0 otherwise).  $\langle \dots \rangle$  represents spatial and ensemble averaging. With this definition,  $\phi$  is therefore the conditional probability of observing a T1 transition at location  $\mathbf{r}_0 + \mathbf{r}$  and time  $t_0 + \Delta t$ , given that a transition has already occurred at  $(\mathbf{r}_0, t_0)$ .

In Fig. 3a, we illustrate the evolution of the field  $\phi$  as  $\Delta t$  increases. The field  $\phi$  behaves like a wave that propagates away from the causal rearrangement and prefers to propagate in the x-direction, coinciding with the direction of the external shear force. The evolution of the field  $\phi$  reflects the interplay between the stress redistribution from a plastic rearrangement and the population of soft spots which could rearrange under the effect of the strain field.

We first focus on the angular dependence of  $\phi$ , which shows an anisotropic four-fold pattern. This anisotropy is consistent with the stress redistribution field due to a rearrangement in an elastic medium as predicted by elastoplastic models [17, 40]. However, it differs from the isotropic probability field observed in ductile, soft disk systems [41]. This contradiction likely arises from the difference in shape anisotropy between soft disks and cells in our system. While soft disk systems exhibit minimal particle shape anisotropy, cells in our system can sustain large deformations and have highly anisotropic shapes. Consequently, deviatoric strain triggers rearrangements in soft disk systems, whereas simple shear strain is responsible for triggering rearrangements in our system.

To better understand how the rearrangement probability field propagates, we looked at  $\phi_x = \frac{\phi(x, y=0)}{\sum_x \phi(x, y=0)}$  and  $\phi_y = \frac{\phi(x=0, y)}{\sum_y \phi(x=0, y)}$  separately.  $\phi_x$ , as observed in Fig. 3b, is a bimodal distribution that evolves in time such that the distance between the two peaks  $d_{peaks}$  increases as time goes. The diffusing bimodal distribution suggests that the propagation is a combination of convection and diffusion, and the drift velocity could be captured by the rate at which the peaks' separation increases. Conversely,  $\phi_y$  is a bell-like shape distribution that gets broader as time progresses (Fig. 3c), indicating that the propagation in the y-direction is similar to a purely diffusion process with the diffusivity can be captured by the evolution of the FWHM. Fig. 3d shows that  $d_{peaks}$  increases faster than the FWHM- $\phi_y$ . Since the rearrangement probability field is the result of the shear stress redistribution and the population of soft spots, the propagating mechanism of the field also should

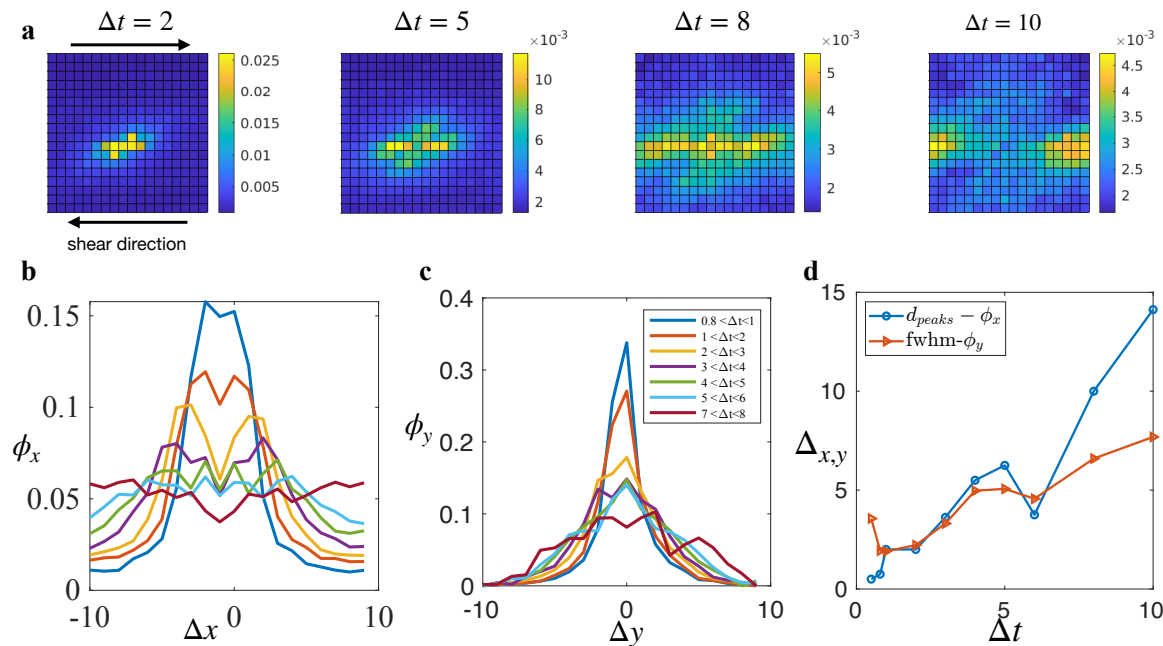


FIG. 3. Propagation of plastic events. **(a)** Evolution of the probability field  $\phi$  at  $p_0 = 3.72$ . Bright regions indicate a high probability of finding another rearrangement in the region relative to the causal rearrangement. **(b)** Spatial distribution of the correlation field  $\phi_x$  as a function of the relative horizontal position  $\Delta x$ . The distribution has a diffusing bimodal shape, indicating a convection process alongside diffusion. **(c)** Spatial distribution of the correlation field  $\phi_y$  as a function of the relative vertical position  $\Delta y$ . The distribution is bell-shaped, with the width of the bell increasing as time progresses, indicating a pure diffusion process. **(d)** The separation of the peaks in  $\phi_x$  and the Full Width at Half Maximum (FWHM) of  $\phi_y$  as functions of the time lag  $\Delta t$ .

agree with the propagation of the stress redistribution.

The phenomenon that the shear stress redistribution tends to propagate in the direction of shear has also been observed in particle-based systems governed by inverse-power-law pairwise potentials [35]. Remarkably, this behavior bears a striking resemblance to the propagation of elastic waves. In the theory of elasticity, longitudinal waves, characterized by displacement in the direction of propagation, outpace transverse waves [42]. Moreover, longitudinal elastic waves involve changes in local density[42], akin to the  $x$ -propagating excitation wave's modulation of local density via T1 transitions. Conversely, transverse elastic waves do not induce density changes, resembling the infrequent involvement of T1 transitions in  $y$ -propagating excitation waves. Notably, the mechanism driving stress redistribution to preferentially propagate in the shear direction appears universal, independent of  $p_0$ . However, since  $p_0$  governs the elastic response in our system, with higher values corresponding to a less elastic state, there is a negative correlation between the stress redistribution wave's speed and  $p_0$ .

#### D. Statistics of tissue avalanches

In addition to the universal propagation mechanism, we wondered if the statistics of tissue yielding events also exhibit universality. In Fig.4a, both the average yielding size  $\bar{S}$ , de-

noting the total number of T1 transitions after a yielding event, and the average stress drop, representing the amount of stress relaxed by the event, exhibit the same dependence on  $p_0$ . In the solid regime, while the stress decreases with increasing  $p_0$ , the average yielding size shows minimal variation. This trend of  $\bar{S}$  versus  $p_0$  is akin to that observed in Fig.1b for the proportion of the solid state.

However, in the marginal phase, there are different types of yielding events as discussed previously (Fig.1c). In the yielding events that occur while the system is fluid-like, illustrated by the **a**  $\rightarrow$  **b** transition in Fig.1C (Type I), the tissue lacks rigidity and therefore is unable to transmit stress to initiate a cascade of rearrangements. Conversely, yielding events following a solid state, illustrated by **c**  $\rightarrow$  **d** and **e**  $\rightarrow$  **f** transitions (Type II), tend to be cascading as the rigid tissue is capable of propagating the stress redistribution. It is this latter type that we refer to as tissue avalanches from now on. Since the avalanches growing mechanism is universal, we expect their statistics to also be independent of  $p_0$ .

Excluding yielding events of type I from the analysis and specifically analyzing only the avalanches, we indeed find that the average avalanche size  $\bar{S}_s$  does not vary significantly with  $p_0$  (Fig.4a inset), suggesting universal avalanche statistics. To rigorously assess this universality, we examine the distribution of avalanche sizes across various  $p_0$  values (see Fig.4b). Strikingly, we observe a consistent power-law distribution, reminiscent of the Gutenberg–Richter (GR) law observed in earthquakes [43, 44], with an exponent  $\tau = -1.36$ ,

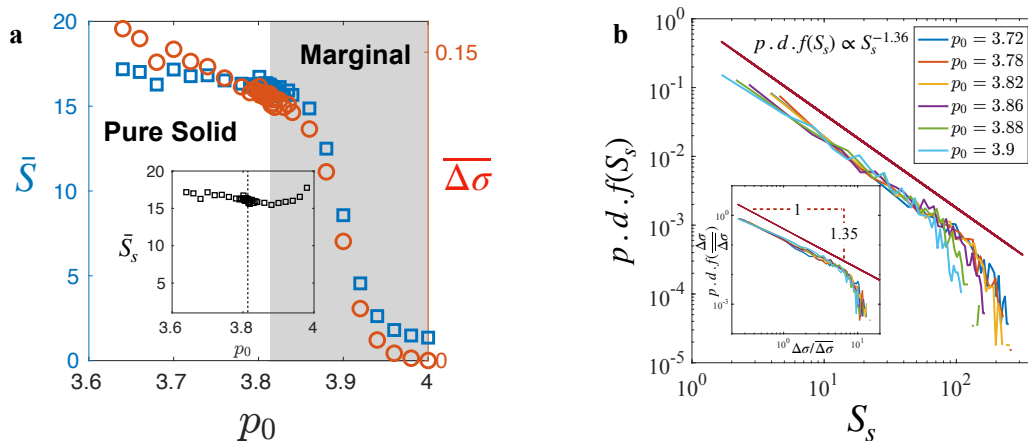


FIG. 4. Avalanches statistics. (a) Dependence of average yielding size  $\bar{S}$  and average stress relaxed  $\overline{\Delta\sigma}$  on  $p_0$ . Inset: Dependence of average avalanches size  $\bar{S}_s$  on  $p_0$ . (b) Distribution of avalanche size follows a power-law distribution. Inset: Distribution of scaled average stress relaxed by avalanches also follows the same power law

which agrees with the analogous exponent observed in overdamped elastoplastic models under shear [45, 46] and in vertex model on spherical surface [47]. This shared characteristic suggests a parallel between biological and seismic avalanches and supports the argument that the vertex model and epithelial tissues belong to the universality class of plastic amorphous systems.

Furthermore, we find that the same power law applies to the distribution of average stress drops during avalanches when scaled by the average (Fig. 4b inset). This collapse after rescaling implies that the stress relaxation mechanism via avalanches is independent of the shape index  $p_0$ , and  $p_0$  only affects the average stress relaxed by governing tissue overall stiffness. Moreover, the similarity in the stress drop distribution and avalanches size distribution indicates that each plastic rearrangement, on average, releases a similar amount of stress that depends only on  $p_0$ . The convergence of these distributions suggests that the growth of avalanches remains unaffected by changes in  $p_0$ , providing additional evidence for the universal propagation mechanism discussed earlier.

### E. Predicting tissue avalanches based on static structural information

While the first cells to undergo a T1 transition triggers the avalanche, in order for the avalanche to grow, it is necessary to have soft spots in the system that are susceptible to undergo T1s. In the framework of the elastoplastic model, it has been established that the distance to yield  $x$ , which represents the additional stress required to trigger a yielding event, follows a power-law distribution,  $p(x) \propto x^{-\theta}$  [48–50]. The exponent  $\theta$  has been suggested as a measure of the system's instability, with a higher value indicating a more stable state.

In the vertex-based model family, it has been proposed that the distance to yield,  $x$ , exhibits a linear relationship with

the length of cell edges, and that the distribution of edge lengths should follow the same power-law behavior as  $p(x)$  [17]. While this argument establishes a connection between system configuration and instability, the efficacy of using the distribution of short edges to describe instability remains uncertain.

To address this ambiguity, we investigate this concept within our Voronoi model and observed an intriguing correlation between the exponent  $\theta$  and system instability (see S.I and Fig.S1). However,  $\theta$  is not a reliable metric because it is derived from a power-law fit that heavily depends on the range of fitting [17]. In practice, the cumulative distribution function (c.d.f) of  $L$  exhibits power-law behavior only within a specific range, which varies from sample to sample. Therefore, we propose using c.d.f( $L^*$ ) as the parameter of instability to avoid the uncertainties and biases associated with fitting. To systematically determine a critical edge length  $L^*$ , we analyzed the evolution of the edge length distribution, c.d.f( $L$ ), at various  $L$  values and compared it with the evolution of tissue shear stress  $\sigma_{xy}$  (Fig. 5a). We observed a critical  $L^*$  at which c.d.f( $L^*$ ), denoted by  $C^*$  from now, exhibited an exceptionally strong correlation with the stress  $\sigma_{xy}$ , with a correlation coefficient exceeding 0.9 (Fig. 5a). Interestingly, we found that  $L^* = 0.43$  (in units of the average cell diameter) remains consistent across different  $p_0$  values.

Given the high correlation between  $C^*$  and  $\sigma$ , and the fact that cell edge lengths can be directly extracted from imaging,  $C^*$  could serve as a non-invasive metric to infer tissue-level stress. Plotting  $C^*$  against  $\sigma_{xy}$  for  $p_0$  in the plastic regime reveals a clear exponential relationship, as shown in Fig. 5b. However, due to the limited range of  $C^*$ , it is challenging to distinguish between an exponential and a power-law relationship. Therefore, we tested both the exponential model ( $\sigma_{xy} \propto e^{\alpha C}$ ) and the power-law model ( $\sigma_{xy} \propto C^\beta$ ). Both models demonstrated a good representation of tissue shear stress (Fig. S4 a, b), with the exponential model exhibiting a slightly lower mean-squared error (MSE) compared to the power-law model (Fig. S4e).

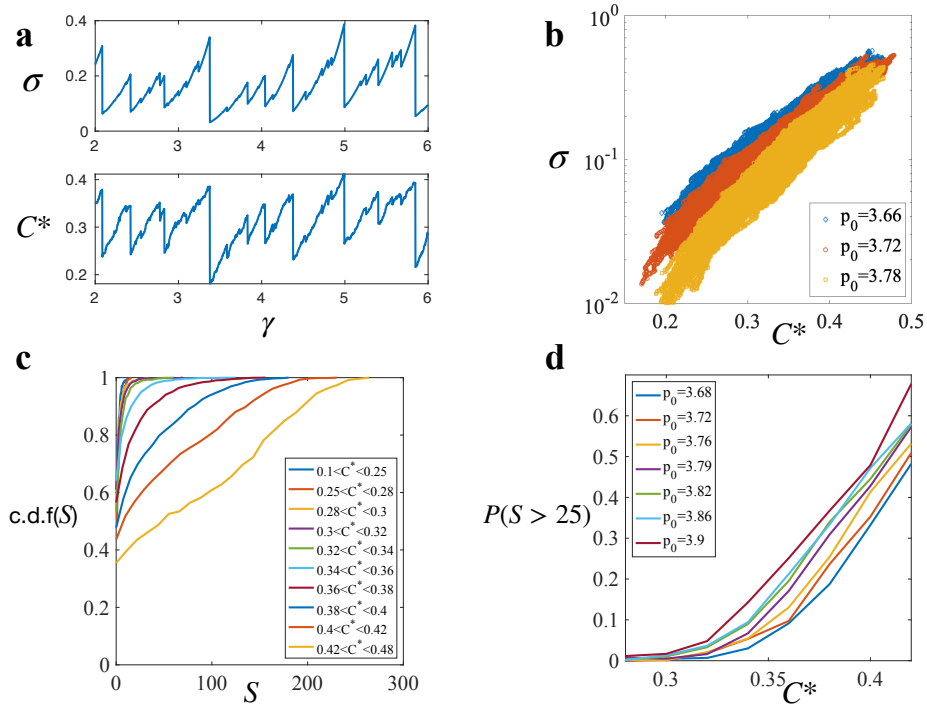


FIG. 5. Predicting avalanches. **(a)** An example of the evolution of tissue shear stress  $\sigma_{xy}$  and  $C^*$  as strain increases. **(b)** Scatter plot of shear stress and  $C^*$  at different  $p_0$  in the solid regime. **(c)** c.d.f( $S$ ) at different  $C^*$  level at  $p_0 = 3.79$ . **(d)** Probability of having avalanches of size greater than 25 at different  $C^*$

Using  $C^*$  as the parameter of instability, with higher  $C^*$  corresponding to a more unstable state, we observed a relationship between instability and avalanche size. By selecting only the failure states, we computed  $C^*$  for these states and then grouped the avalanche sizes based on  $C^*$  at the point of failure (Fig.5c). At low  $C^*$ , if the tissue yields, the size of the yielding event is likely to be small, indicated by a rapid increase to 1 in the cumulative distribution function (c.d.f.) of  $S$ . As  $C^*$  increases, the likelihood of larger yield events grows. The probability of observing an avalanche of size 25 or greater is summarized in Fig.5d.

While  $C^*$  can provide predictions about avalanche size, it cannot determine when an avalanche will occur. Therefore, we require another tool to forecast yielding events. In amorphous solids, the locations of plastic rearrangements during an avalanche largely depend on the material's structural configuration, with areas more likely to experience plastic events called soft spots. Various frameworks have been proposed to link structure and plasticity, such as the Shear Transformation Zone theory [37–39, 51, 52] and lattice-based models. The most promising theoretical approach for predicting the locations of soft spots involves identifying these areas based on soft vibrational modes [36, 53, 54]. As a system approaches a plastic rearrangement, at least one normal mode is supposed to approach zero frequency [36]. However, the vibrational mode analysis is not applicable to the vertex-based model family due to the cuspleness of the energy landscape [20, 32]. In such systems, the energy cusp at a plastic event prevents the corresponding low-frequency mode from vanishing as it would in

systems with smooth, analytic energy landscape. As shown in Fig.S2, in our system, no low-frequency mode approaches zero frequency except at the onset of the plastic event. Hence, an alternative approach is necessary.

In our model, the deformation of edges immediately following shear strain is deterministic. Through simple geometry, we deduce the existence of a range of orientations wherein edges are prone to shortening upon shearing, rendering them more vulnerable. In the vertex model, under the condition  $\dot{\gamma} \ll 1$ , the change in edge length  $\delta l$  due to shear is approximated as  $\delta l \approx \dot{\gamma} l \sin(2\phi)$ , where  $l$  and  $\phi$  represent the edge length and orientation, respectively. Consequently, in the vertex model, the most vulnerable orientation is  $\frac{3\pi}{4}$ . If an edge is sufficiently weak (or short) and happens to align with this susceptible orientation, it may yield under the influence of shearing, potentially triggering further rearrangements in its vicinity. We refer to these susceptible edges as triggers. Since triggers are local elements, their presence is not captured by the cumulative distribution function of edge lengths, c.d.f( $L$ ), thereby explaining why  $C^*$  alone cannot predict imminent system failure. In summary, the presence of a trigger is the necessary condition, while a high  $C^*$  in the current state is the sufficient condition for a large avalanche in a tissue monolayer.

### III. DISCUSSION

We studied the response of tissue monolayers to external quasi-static shear stress in the long-term steady-shear regime. For a tissue monolayer initially in a fluid state, it behaves like a yield-stress material in the shear buildup regime but eventually enters a marginal phase in the long-term steady shear regime. Incorporating the coexistence phase into the SGR model, we elucidated the discrepancy between the rigidity transition and the yield stress transition observed in the Vertex model under simple shear.

Besides the yield stress, tissue plasticity is also reflected in avalanches of plastic rearrangement. By studying the dynamics of tissue avalanches, we observed a universal propagation mechanism of plastic events that is independent of the shape index  $p_0$  and has two preferred directions, with the direction of the external shear being the one with faster propagation. The rearrangement probability  $\phi$  studied here is closely related to, but not identical with, the stress redistribution predicted by elastoplastic models [17, 40] or the strain field due to rearrangement [41]. Instead,  $\phi$  captured the interplay between stress redistribution and spatial distribution of weak spots. Since most edges that participated in T1 transition in our system orient at  $-\pi/4$  with respect to the horizontal (Fig.S3), the positive shear stress is expected to symmetrically redistribute along the horizontal and vertical directions [17]. Although  $\phi$  does propagate mainly in the horizontal and vertical directions, it does not possess the vertical-horizontal symmetry seen in stress redistribution or in the strain field. This difference arises from highly heterogeneity and anisotropic in the spatial distribution of weak spots.

The universality of tissue avalanches is not only reflected in the propagation of plastic events but also captured by a power-law distribution of avalanche sizes, with an exponent  $\tau = -1.36$ , strengthening the argument that epithelial tissues behave like plastic amorphous materials. We also propose a metric to not only predict tissue avalanches but also infer tissue stress in highly anisotropic systems based on an instantaneous static snapshot. In finite size system, the cut off avalanches size  $S_c$  depends on the system size  $N$  as  $S_c \propto N^{d_f/d}$ , where  $d_f$  is avalanches fractal dimension and  $d$  is the dimension of the system [49]. Future possible work can be performed with different system size to obtain the avalanches fractal dimension  $d_f$  and further understand the finite size effect on avalanches.

We also propose a metric to not only infer tissue stress based on an instantaneous static snapshot but also predict tissue avalanches. Quantification of tissue-level force and stress is necessary to understand the physics of many biological processes. However, direct measurement of stress in vivo is considerably challenging [55–57]. Compared to other non-invasive method to estimate tissue stress such as Bayesian Force Inference [58] and Variational Method for Image-Based Inference [59], our approach using  $C^*$  offers a simple and fast method to estimate tissue stress. The cost for this convenience is that our approach cannot provide a spatial distribution of stress. The strong agreement between  $\sigma_{xy}$  and  $C^*$  is noteworthy, especially since  $C^*$  does not incorporate informa-

tion about edge orientation, which directly affects stress. In an isotropic system, edge length alone is insufficient to infer stress. However, in a system undergoing large deformation and thus highly anisotropic, the influence of edge orientation diminishes, making edge length alone sufficient for stress inference. The impact of shape anisotropy is evident during the buildup phase or when the system is in a fluid state. In these scenarios, edges may have negligible tension, making edge tension independent of edge length. Consequently, it is possible that systems with similar  $C^*$  values could exhibit significantly different stress levels.

The impact of triggers on avalanches goes beyond simply initiating them; we observed a significant dependence of avalanche size on the trigger location. By manually shrinking vanishing edges at various locations within the same configuration, we noted that the size of the resulting avalanches varied markedly. This indicates that the location of the initial excitation has a profound influence on the final size of the avalanche. A promising future research direction could involve developing a theoretical framework that moves beyond the mean field approach to more accurately capture the spatial heterogeneity in the tissue.

### ACKNOWLEDGMENTS

We thank Craig E. Maloney, Marko Popovic, and Jie Lin for insightful discussions. We acknowledge support from the National Science Foundation (grant nos. DMR-2046683 and PHY-2019745), the Alfred P. Sloan Foundation, the Human Frontier Science Program (Ref.-No.: RGP0007/2022), the NIGMS of the National Institutes of Health (NIH) under award number R35GM15049, and the Northeastern University Discovery Cluster.

### MATERIALS AND METHOD

#### Simulation Model

To numerically study the behavior of dense epithelial tissues under large deformation, we use a Voronoi-based version [18] of the Vertex Model [60], where the degrees of freedom are the set of cell centers denoted as  $\{\mathbf{r}_i\}$  and the geometric configurations of cells are derived from their respective Voronoi tessellation. The biomechanics governing interactions both within and between cells can be effectively represented at a coarse-grained level [19, 61], expressed in terms of a mechanical energy functional associated with cell shapes, given by:

$$E = \sum_{i=1}^N [K_A(A_i - A_0)^2 + K_P(P_i - P_0)^2], \quad (7)$$

where  $A_i$  and  $P_i$  represent the area and perimeter of the  $i$ -th cell, respectively. The parameters  $K_A$  and  $K_P$  denote the area and perimeter moduli, respectively. The values  $A_0$  and  $P_0$  correspond to the preferred area and perimeter values, with  $A_0$



specifically set to the average area per cell  $\bar{A}$ . Without the loss of generality, we choose  $K_P A_0$  as the energy unit and  $\sqrt{A_0}$  as the length unit. This leads to the dimensionless form of the energy

$$\varepsilon = \sum_{i=1}^N \kappa_A (a_i - 1)^2 + (p_i - p_0)^2, \quad (8)$$

where  $\kappa_A = K_A A_0 / K_P$  represents the rescaled area elasticity, governing the cell area stiffness relative to the perimeter stiffness and  $p_0 = P_0 / \sqrt{A_0}$  the cell shape index. To investigate the mechanical response of the tissue, we apply simple-shear deformation to the simulated tissues utilizing Lees-Edwards boundary conditions [62]. Initially, strain-free configurations ( $\gamma = 0$ ) are generated with randomly distributed cell centers. The FIRE algorithm [63] is subsequently employed to minimize the energy functional in accordance with Eq. 8. Strain is then incrementally applied in steps of  $\Delta\gamma = 2 \times 10^{-3}$  until reaching a maximum value of  $\gamma_{max} = 6$ . Alongside the modification of periodic boundary conditions to account for the strain, an affine displacement field  $\Delta \mathbf{r}_i = \Delta\gamma y_i \hat{x}$  is applied to the cell centers. Following each increment of strain, the FIRE algorithm is again utilized to minimize the energy functional (Eq.8) until the residual forces acting on cell centers fall below  $10^{-14}$ , so that all resultant tissue states are metastable. This procedural approach effectively corresponds to investigating the system within the athermal quasi-static limit ( $\dot{\gamma} \rightarrow 0$ ). The tissues under examination encompass cell populations  $N = 400$ , accompanied by cell shape indices  $p_0$  varying between 3.7 and 4, and a total of 84 random initial samples were simulated at each set of parameter values.

We calculate the tension, denoted as  $\mathbf{T}_{ij}$ , acting along an edge  $\mathbf{l}_{ij}$  shared by cells  $i$  and  $j$  using the equation [58, 64, 65]

$$\mathbf{T}_{ij} = \frac{\partial \varepsilon}{\partial \mathbf{l}_{ij}} = 2[(p_i - p_0) + (p_j - p_0)] \hat{\mathbf{l}}_{ij}, \quad (9)$$

where  $\hat{\mathbf{l}}_{ij}$  represents the unit vector along  $\mathbf{l}_{ij}$ . Furthermore, the global tissue shear stress  $\boldsymbol{\sigma}$  can be obtained by

$$\boldsymbol{\sigma} = \boldsymbol{\sigma}_{xy} \equiv \frac{1}{N} \sum_{i < j} T_{ij}^x l_{ij}^y, \quad (10)$$

where  $T_{ij}^x$  denotes the  $x$ -component of  $\mathbf{T}_{ij}$  and  $l_{ij}^y$  stands for the  $y$ -component of  $\mathbf{l}_{ij}$ .

## APPENDIX

### Computing tissue level mechanical linear response

The tissue level mechanical response was quantified by the shear modulus  $G$ . We computed  $G$  using Born-Huang formulation in the limit of infinitesimal affine strain  $\gamma$  [66, 67]:

$$G = \frac{1}{A_{total}} \left( \frac{\partial^2 E}{\partial \gamma^2} - \Xi_{i\alpha} H_{i\alpha j\beta}^{-1} \Xi_{j\beta} \right), \quad (S.1)$$

where the Roman indexes  $i, j$  label cells and Greek indexes  $\alpha, \beta$  denote Cartesian components.  $\Xi_{i\alpha}$  is the derivative of the force on cell  $i$ th with respect to the strain  $\gamma$ :

$$\Xi_{i\alpha} = \frac{\partial^2 E}{\partial r_{i\alpha} \partial \gamma} \quad (S.2)$$

$H$  is the Hessian matrix given by the second derivative of the tissue energy  $E$  with respect to position cells position:

$$H_{i\alpha j\beta} = \frac{\partial^2 E}{\partial r_{i\alpha} \partial r_{j\beta}} \quad (S.3)$$

### Steady state solution and asymptotic behavior in dual-state SGR

In the Fokker-Planck equation of motion Eqn. 3, the total yielding rate  $\Gamma(t)$  is given by [28]:

$$\Gamma(t) = \Gamma_0 \int dE dl P(E, l, t) \exp \left[ -\frac{E - kl^2/2}{x} \right]. \quad (S.4)$$

Since we are interested in the long-term steady shear, we look for a steady state solution to Eqn. 3. In steady state, Eqn. 3 becomes an ODE with respect to  $l$ :

$$\frac{\partial P}{\partial l} + \frac{\Gamma_0}{\dot{\gamma}} \exp \left[ -\frac{E - kl^2/2}{x} \right] P = \frac{\Gamma}{\dot{\gamma}} \rho(E) \delta(l)$$

The steady-state solution is [28]:

$$P(E, l) = \frac{\Gamma}{\dot{\gamma}} \rho(E) \exp(-ze^{-E/x}) \quad (S.5)$$

Where  $z(l)$  is:

$$z(l) = \frac{\Gamma_0}{\dot{\gamma}} \int_0^l dl' e^{kl'^2/2x} \quad (S.6)$$

In steady state, the total yielding rate  $\Gamma$  is just a constant and can be found by normalizing  $P(E, l)$ , giving the steady state solution for  $P(E, l)$  of the form:

$$P(E, l) = \frac{\rho(E) \exp(-ze^{-E/x})}{\int_0^\infty dl G_\rho(z)}$$

Where  $G_\rho$  is:

$$G_\rho(z) = \int_0^\infty dE \rho(E) \exp(-ze^{-E/x})$$

$G_\rho$  can be separated into two parts. The first part, denoted by  $G_\delta$ , comes from the contribution of the zero energy traps (the Dirac-delta function in  $\rho(E)$ ).  $G_\Gamma$  denotes the second part coming from the non-zero energy traps (the Gamma function in  $\rho(E)$ ):

$$G_\delta(z) = \int dE \delta(E) \exp(-ze^{-E/x}) = \exp(-z)$$

$$G_\Gamma(z) = \int dE \frac{E^{\kappa-1} e^{-E/x_0}}{\Gamma(\kappa) x_0^\kappa} \exp(-ze^{-E/x})$$

$$G_\rho(z) = f_0 G_\delta + (1 - f_0) G_\Gamma$$

The steady-state solution in the long-time limit can be studied more conveniently using the following auxiliary functions:

$$\begin{aligned} I_{0\delta} &= \int dl G_\delta \\ I_{1\delta} &= k_\delta \int dl l G_\delta \approx 0 \\ I_{0\Gamma} &= \int dl G_\Gamma \\ I_{1\Gamma} &= k \int dl l G_\Gamma \end{aligned}$$

Since our main focus is the rheological response of the system, reflected in the macroscopic stress, we compute the system stress by ensemble averaging the local stress [28]:

$$\sigma = \langle kl \rangle = \int \int dE dl k l P(E, l) \quad (\text{S.7})$$

Using the auxiliary functions and the steady-state solution, the stress is therefore given by:

$$\sigma = \frac{(1 - f_0) I_{1\Gamma}}{f_0 I_{0\delta} + (1 - f_0) I_{0\Gamma}} \quad (\text{S.8})$$

For an element with zero yielding energy, the strain of the element is of order  $\frac{\dot{\gamma}}{\Gamma_0}$ . Therefore, in the low strain-rate limit, the strain of the element with zero yield energy is typically small so  $G_\delta$  can be approximated in this limit as:

$$G_\delta = \exp(-l\Gamma_0/\dot{\gamma})$$

In the case of  $\kappa = 2$  and let  $\chi = \frac{x}{x_0} < 2$ , using the substitution  $u = e^{-E/x}$  and integration by part,  $G_\Gamma(z)$  can be integrated as follow:

$$\begin{aligned} G_\Gamma(z) &= \int_1^0 \chi^2 \ln(u) u^{\chi-1} \exp(-zu) du \\ &= \frac{\chi^2 (\chi - 1)!}{z^\chi} \sum_{n=1}^{\infty} \frac{(-z)^n}{n n!} \end{aligned}$$

The series  $\sum_{n=1}^{\infty} \frac{(-z)^n}{n n!}$  converges by alternating series test and therefore  $G_\Gamma(z)$  scales as  $z^{-\chi}$ . We then obtain the following scaling relations:

$$I_{0\delta} \approx \dot{\gamma}/\Gamma_0 \quad (\text{S.9})$$

$$I_{0\Gamma} \approx C(\chi) \dot{\gamma}^\chi \quad (\text{S.10})$$

$$I_{1\Gamma} \approx D(\chi) \dot{\gamma}^\chi \quad (\text{S.11})$$

Using, the steady state solution, the proportion of time that elements spends in the zero yielding energy traps (fluid state)  $P$  can be expressed in terms of  $f_0$ :

$$P = \frac{f_0 I_{0\delta}}{f_0 I_{0\delta} + (1 - f_0) I_{0\Gamma}} \quad (\text{S.12})$$

Combining Eq. S.8 and Eq. S.12, the yield stress can be calculated as:

$$\sigma_y(x) = \frac{(1 - f_0) I_{1\Gamma}}{f_0 I_{0\delta} + (1 - f_0) I_{0\Gamma}} = (1 - P) \frac{I_{1\Gamma}}{I_{0\Gamma}} = (1 - P) \sigma_0 \quad (\text{S.13})$$

Where  $\sigma_0$  is the yield stress that arises solely from elements in a solid state, which is finite based on the scaling relation S.10 and S.11.

## AN EXPONENT OF INSTABILITY

We extract the instability exponent,  $\theta$ , from the cumulative distribution function (c.d.f) of edge lengths, denoted as c.d.f( $L$ ), by fitting a power law to c.d.f( $L$ ) in the interval  $0.05 < L < 0.5$ . This interval specifically represents the short edges that are capable of undergoing T1 transitions.

We focused on tissues exclusively in the solid regime (shape index  $p_0$  less than 3.81) and integrated this understanding with the dual-state coexistence proportion to extend the analysis to higher shape indices. For purely solid tissues, as stress builds up, the instability exponent  $\theta$  gradually decreases. Conversely, when stress is relieved through avalanches,  $\theta$  experiences a sharp increase (S1a), indicating that a significant number of soft spots are relaxed, making the system considerably more stable.

Furthermore, the  $\theta$  exponent is correlated with avalanche properties, as evidenced by its relationship with the average avalanche size ( $\bar{s}$ ) and the probability of avalanche occurrence. Systems with a lower  $\theta$  exponent, indicating greater instability, tend to experience larger avalanches on average (Figure S1b) and are more prone to yielding (Figure S1b inset).

## NORMAL MODES ARE UNABLE TO IDENTIFY THE SOFT SPOTS IN THE VERTEX-BASED MODEL

In amorphous solids, localization plays a crucial role in understanding the rheology of the material. An example of localization is shear transformation zone (STZ) [37–39, 51, 52], localized regions in which sudden and irreversible rearrangements occur when the material is subjected to shear. These STZ, also referred to as weak spots, can interact and lead to avalanches of irreversible plastic events, making the identification of these weak spots in disordered systems a crucial and challenging task. Research has indicated that the local yield stress could serve as a reliable predictor for these weak spots [37]. However, locally probing the system is impractical and does not align with our objective of making predictions based solely on current and historical snapshots. Another approach to this task involves analyzing the normal mode of the system near failure. Studies on systems of harmonic repulsive particles have demonstrated that low-frequency modes typically correspond to low energy barriers [68], making them dominant modes during a plastic event [68–70]. Furthermore, in systems with explicit separation dependence potential (such as Hertzian and Lennard-Jones potentials), under the quasistatic limit, the evolution of low-frequency modes follows a distinct pattern: as the system approaches failure, a gradual decrease in frequency towards zero is anticipated [36, 70].

To see whether the normal modes of the Hessian could help to identify failure events, whenever there is a known avalanche

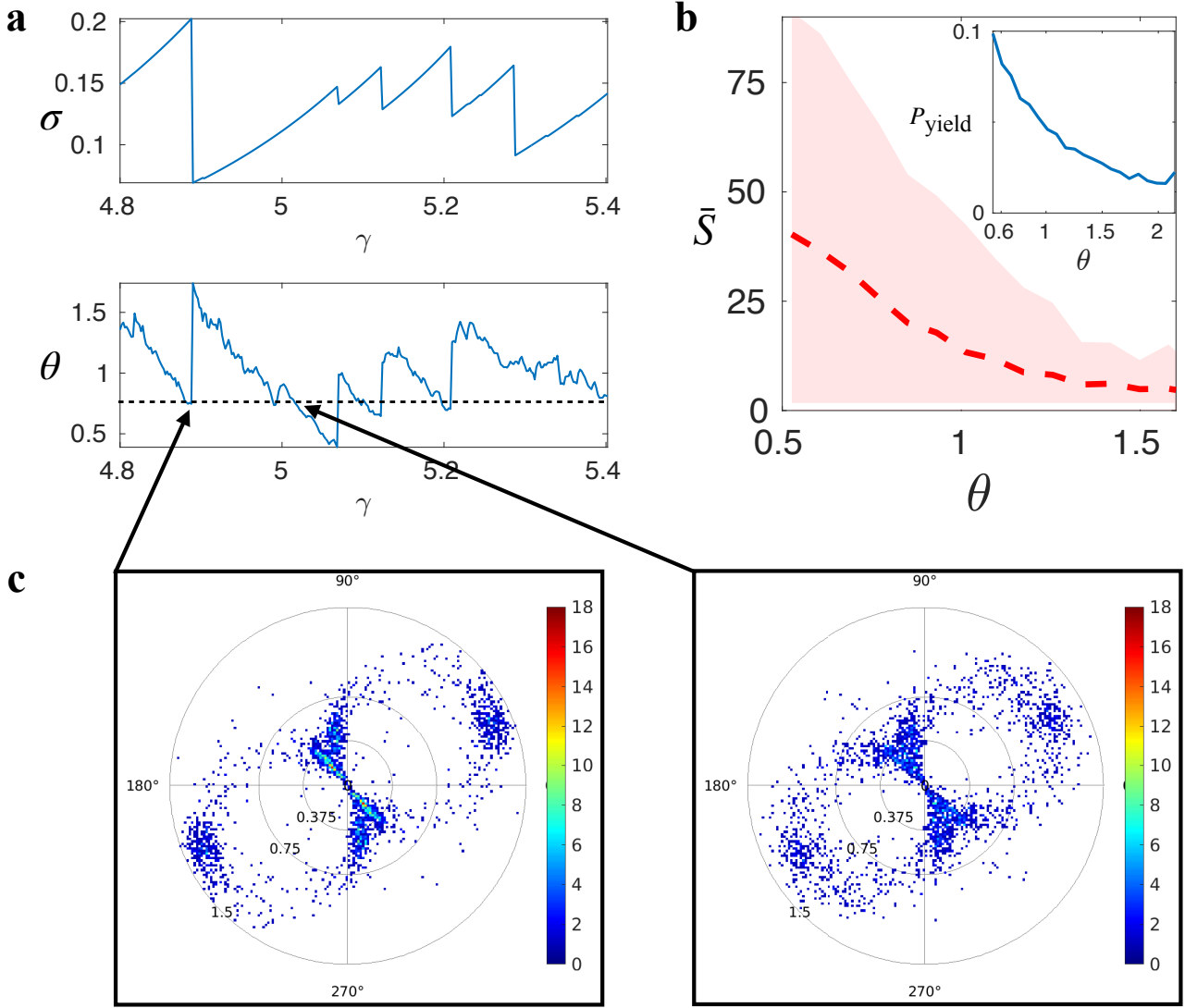


FIG. S1. A proposed exponent of instability. (a) An example of the evolution of tissue shear stress  $\sigma_{xy}$  and  $\theta$  exponent as strain increases. (b) Dependence of average avalanche size and the exponent of instability  $\theta$ . Inset: the probability to yield  $\rho_+$  versus  $\theta$ . (c) The polar distribution of edges vector in an unstable and stable configuration. Data shown in Figure 3 is extracted from a system with shape index  $p_0 = 3.74$  in the solid regime.

in our simulation, we rerun the simulation starting at this particular strain but with the strain step decreased by 100 times and let the system approach to the avalanche again in the more detailed fashion. The low-frequency modes at the starting strain were then extracted from the Hessian. To keep track of the mode while the system evolves, we found the most similar mode to these starting low-frequency modes at each step and used them to represent the starting modes using the overlapping function  $\Omega = \mathbf{e}_i \cdot \mathbf{e}_j$ , where  $\mathbf{e}_i$  and  $\mathbf{e}_j$  are eigenvectors of comparison. The overlap is shown on the right panel of Figure S2. In contrast to what was observed in other systems, we did not see a gradual decrease in the low-frequency mode eigenvalues. Instead, it is always a sharp decrease but not zero right at the onset of avalanches, no matter how detailed we zoom in on the approaching process. This non-smooth sudden drop

in the eigenvalues at the onset of avalanches arises from the cuspsiness of the energy landscape. Because of the cuspsiness, there is no saddle point when the system approaches a rearrangement event and therefore the curvature is always positive.

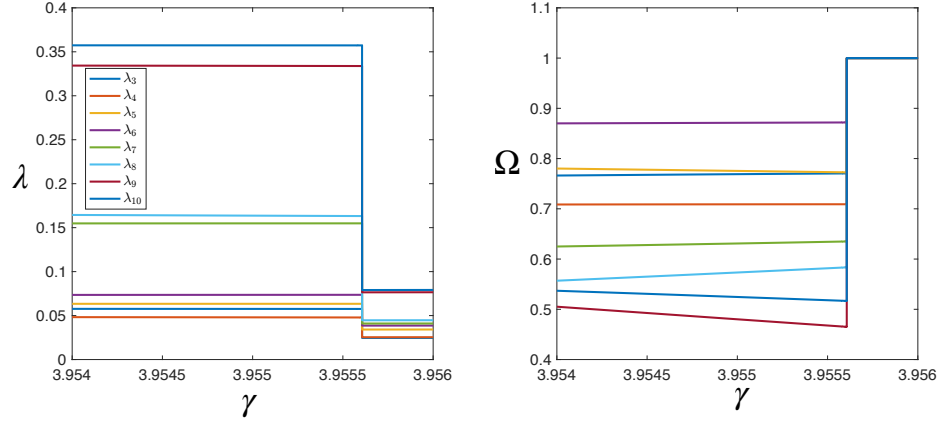


FIG. S2. Evolution of low-frequency mode near avalanches.

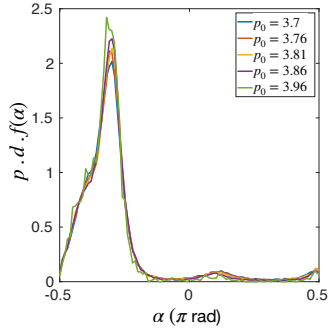


FIG. S3. The orientation distribution of T1-edges (edges undergo T1 transitions) at various values of  $p_0$ .

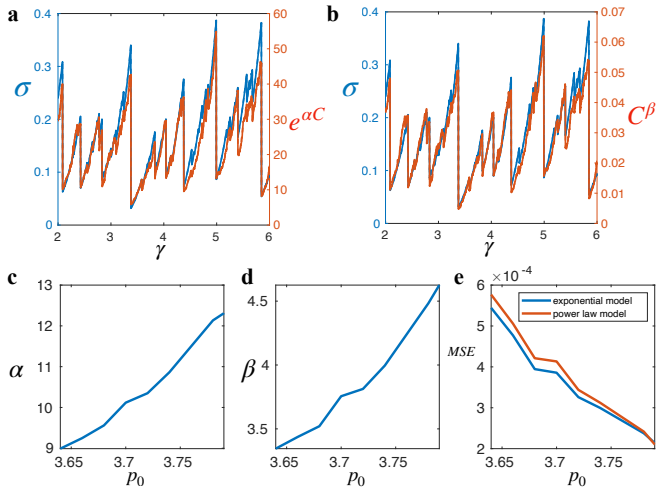


FIG. S4. Fitting  $\sigma_{xy}$  vs  $C^*$  to exponential and power-law model.

[1] A. Bonfanti, J. Duque, A. Kabla, and G. Charras, Fracture in living tissues, Trends in Cell Biology **32**, 537 (2022).

[2] E. Sadeghipour, M. A. Garcia, W. J. Nelson, and B. L. Pruitt,

- Shear-induced damped oscillations in an epithelium depend on actomyosin contraction and e-cadherin cell adhesion, *eLife* **7**, 10.7554/eLife.39640 (2018).
- [3] Y. Bashirzadeh, S. Dumbali, S. Qian, and V. Maruthamuthu, Mechanical response of an epithelial island subject to uniaxial stretch on a hybrid silicone substrate, *Cellular and Molecular Bioengineering* **12**, 33 (2018).
- [4] G. Cai, A. Nguyen, Y. Bashirzadeh, S.-S. Lin, D. Bi, and A. P. Liu, Compressive stress drives adhesion-dependent unjamming transitions in breast cancer cell migration, *Frontiers in Cell and Developmental Biology* **10**, 10.3389/fcell.2022.933042 (2022).
- [5] A. R. Harris, L. Peter, J. Bellis, B. Baum, A. J. Kabla, and G. T. Charras, Characterizing the mechanics of cultured cell monolayers, *Proceedings of the National Academy of Sciences* **109**, 16449 (2012).
- [6] F. Villemot and M. Durand, Quasistatic rheology of soft cellular systems using the cellular potts model, *Physical Review E* **104**, 055303 (2021).
- [7] A. Merzouki, O. Malaspinas, and B. Chopard, The mechanical properties of a cell-based numerical model of epithelium, *Soft Matter* **12**, 4745 (2016).
- [8] J. Huang, J. O. Cochran, S. M. Fielding, M. C. Marchetti, and D. Bi, Shear-driven solidification and nonlinear elasticity in epithelial tissues, *Physical Review Letters* **128**, 178001 (2022).
- [9] M. J. Hertaeg, S. M. Fielding, and D. Bi, Discontinuous shear thickening in biological tissue rheology, *Physical Review X* **14**, 011027 (2024).
- [10] S. S. Lienkamp, K. Liu, C. M. Karner, T. J. Carroll, O. Ronneberger, J. B. Wallingford, and G. Walz, Vertebrate kidney tubules elongate using a planar cell polarity-dependent, rosette-based mechanism of convergent extension, *Nature genetics* **44**, 1382 (2012).
- [11] R. Etoynay, M. Popović, M. Merkel, A. Nandi, C. Blasse, B. Aigouy, H. Brandl, G. Myers, G. Salbreux, F. Jülicher, and S. Eaton, Interplay of cell dynamics and epithelial tension during morphogenesis of the *Drosophila* pupal wing, *eLife* **4**, e07090 (2015).
- [12] E. Heller, K. V. Kumar, S. W. Grill, and E. Fuchs, Forces generated by cell intercalation tow epidermal sheets in mammalian tissue morphogenesis, *Developmental Cell* **28**, 617 (2014).
- [13] S. Curran, C. Strandkvist, J. Bathmann, M. de Gennes, A. Kabla, G. Salbreux, and B. Baum, Myosin ii controls junction fluctuations to guide epithelial tissue ordering, *Developmental Cell* **43**, 480 (2017).
- [14] A. Ruina, Slip instability and state variable friction laws, *Journal of Geophysical Research: Solid Earth* **88**, 10359 (1983).
- [15] P. Bak, C. Tang, and K. Wiesenfeld, Self-organized criticality: An explanation of the  $1/f$  noise, *Physical review letters* **59**, 381 (1987).
- [16] G. Courcoubetis, C. Xu, S. V. Nuzhdin, and S. Haas, Avalanches during epithelial tissue growth; uniform growth and a drosophila eye disc model, *PLOS Computational Biology* **18**, e1009952 (2022).
- [17] M. Popović, V. Druelle, N. A. Dye, F. Jülicher, and M. Wyart, Inferring the flow properties of epithelial tissues from their geometry, *New Journal of Physics* **23**, 033004 (2021).
- [18] D. Bi, X. Yang, M. C. Marchetti, and M. L. Manning, Motility-driven glass and jamming transitions in biological tissues, *Phys. Rev. X* **6**, 021011 (2016).
- [19] D. B. Staple, R. Farhadifar, J. C. Röper, B. Aigouy, S. Eaton, and F. Jülicher, Mechanics and remodelling of cell packings in epithelia, *The European Physical Journal E* **33**, 117 (2010).
- [20] D. Bi, J. H. Lopez, J. M. Schwarz, and M. L. Manning, A density-independent rigidity transition in biological tissues, *Nature Physics* **11**, 10741079 (2015).
- [21] D. Bi, J. Zhang, B. Chakraborty, and R. P. Behringer, Jamming by shear, *Nature* **480**, 355 (2011).
- [22] R. P. Behringer and B. Chakraborty, The physics of jamming for granular materials: a review, *Reports on Progress in Physics* **82**, 012601 (2018).
- [23] V. Babu and S. Sastry, Criticality and marginal stability of the shear jamming transition of frictionless soft spheres, *Physical Review E* **105**, L042901 (2022).
- [24] V. Babu, H. Vinutha, D. Bi, and S. Sastry, Discontinuous rigidity transition associated with shear jamming in granular simulations, *Soft Matter* **19**, 9399 (2023).
- [25] P. Shah, S. Arora, and M. M. Driscoll, Coexistence of solid and liquid phases in shear jammed colloidal drops, *Communications Physics* **5**, 222 (2022).
- [26] J. F. Morris, Shear thickening of concentrated suspensions: Recent developments and relation to other phenomena, *Annual Review of Fluid Mechanics* **52**, 121 (2020).
- [27] P. Sollich, F. Lequeux, P. Hébraud, and M. E. Cates, Rheology of soft glassy materials, *Physical Review Letters* **78**, 2020 (1997).
- [28] P. Sollich, Rheological constitutive equation for a model of soft glassy materials, *Physical Review E* **58**, 738 (1998).
- [29] G. Yin and M. J. Solomon, Soft glassy rheology model applied to stress relaxation of a thermoreversible colloidal gel, *Journal of Rheology* **52**, 785 (2008).
- [30] D. Bonn, P. Coussot, H. T. Huynh, F. Bertrand, and G. Debrégeas, Rheology of soft glassy materials, *Europhysics Letters (EPL)* **59**, 786 (2002).
- [31] K. K. Mandadapu, S. Govindjee, and M. R. Mofrad, On the cytoskeleton and soft glassy rheology, *Journal of Biomechanics* **41**, 1467 (2008).
- [32] D. Bi, J. H. Lopez, J. M. Schwarz, and M. L. Manning, Energy barriers and cell migration in densely packed tissues, *Soft Matter* **10**, 1885 (2014).
- [33] J. R. Samaniuk, E. Hermans, T. Verwijlen, V. Pauchard, and J. Vermant, Soft-glassy rheology of asphaltenes at liquid interfaces, *Journal of Dispersion Science and Technology* **36**, 1444 (2015).
- [34] E. Stanifer and M. L. Manning, Avalanche dynamics in sheared athermal particle packings occurs via localized bursts predicted by unstable linear response, *Soft Matter* **18**, 2394–2406 (2022).
- [35] D. Richard, A. Elgailani, D. Vandembroucq, M. L. Manning, and C. E. Maloney, Mechanical excitation and marginal triggering during avalanches in sheared amorphous solids, *Physical Review E* **107**, 034902 (2023).
- [36] M. L. Manning and A. J. Liu, Vibrational modes identify soft spots in a sheared disordered packing, *Phys. Rev. Lett.* **107**, 108302 (2011).
- [37] S. Patinet, D. Vandembroucq, and M. L. Falk, Connecting local yield stresses with plastic activity in amorphous solids, *Physical Review Letters* **117**, 10.1103/physrevlett.117.045501 (2016).
- [38] M. L. Falk and J. S. Langer, Dynamics of viscoplastic deformation in amorphous solids, *Physical Review E* **57**, 7192 (1998).
- [39] M. L. Manning, J. S. Langer, and J. M. Carlson, Strain localization in a shear transformation zone model for amorphous solids, *Physical Review E* **76**, 10.1103/physreve.76.056106 (2007).
- [40] G. Picard, A. Ajdari, F. Lequeux, and L. Bocquet, Elastic consequences of a single plastic event: A step towards the microscopic modeling of the flow of yield stress fluids, *The European Physical Journal E* **15**, 371 (2004).
- [41] G. Zhang, S. A. Ridout, and A. J. Liu, Interplay of rearrangements, strain, and local structure during avalanche propagation, *Physical Review X* **11**, 041019 (2021).

- [42] L. D. Landau, L. Pitaevskii, A. M. Kosevich, and E. M. Lifshitz, *Theory of elasticity: volume 7*, Vol. 7 (Elsevier, 1959) pp. 87–89.
- [43] H. Kawamura, T. Hatano, N. Kato, S. Biswas, and B. K. Chakrabarti, Statistical physics of fracture, friction, and earthquakes, *Reviews of Modern Physics* **84**, 839–884 (2012).
- [44] B. Gutenberg and C. F. Richter, Frequency of earthquakes in California, *Bulletin of the Seismological society of America* **34**, 185 (1944).
- [45] M. Talamali, V. Petäjä, D. Vandembroucq, and S. Roux, Avalanches, precursors, and finite-size fluctuations in a mesoscopic model of amorphous plasticity, *Physical Review E* **84**, 016115 (2011).
- [46] K. Karimi, E. E. Ferrero, and J.-L. Barrat, Inertia and universality of avalanche statistics: The case of slowly deformed amorphous solids, *Physical Review E* **95**, 013003 (2017).
- [47] A. Amiri, C. Duclut, F. Jülicher, and M. Popović, Random traction yielding transition in epithelial tissues, *Physical Review Letters* **131**, 188401 (2023).
- [48] J. Lin and M. Wyart, Mean-field description of plastic flow in amorphous solids, *Physical Review X* **6**, 10.1103/physrevx.6.011005 (2016).
- [49] J. Lin, E. Lerner, A. Rosso, and M. Wyart, Scaling description of the yielding transition in soft amorphous solids at zero temperature, *Proceedings of the National Academy of Sciences* **111**, 14382–14387 (2014).
- [50] J. Lin, A. Saade, E. Lerner, A. Rosso, and M. Wyart, On the density of shear transformations in amorphous solids, *EPL (Europhysics Letters)* **105**, 26003 (2014).
- [51] D. Richard, G. Kapteijns, J. A. Giannini, M. L. Manning, and E. Lerner, Simple and broadly applicable definition of shear transformation zones, *Physical Review Letters* **126**, 10.1103/physrevlett.126.015501 (2021).
- [52] J. LANGER, Shear-transformation-zone theory of deformation in metallic glasses, *Scripta Materialia* **54**, 375–379 (2006).
- [53] J. Rottler, S. S. Schoenholz, and A. J. Liu, Predicting plasticity with soft vibrational modes: From dislocations to glasses, *Physical Review E* **89**, 042304 (2014).
- [54] J. Ding, S. Patinet, M. L. Falk, Y. Cheng, and E. Ma, Soft spots and their structural signature in a metallic glass, *Proceedings of the National Academy of Sciences* **111**, 14052 (2014).
- [55] K. Haase and A. E. Pelling, Investigating cell mechanics with atomic force microscopy, *Journal of The Royal Society Interface* **12**, 20140970 (2015).
- [56] K. Bambardekar, R. Clément, O. Blanc, C. Chardès, and P.-F. Lenne, Direct laser manipulation reveals the mechanics of cell contacts in vivo, *Proceedings of the National Academy of Sciences* **112**, 1416 (2015).
- [57] I. Bonnet, P. Marcq, F. Bosveld, L. Fetler, Y. Bellaïche, and F. Graner, Mechanical state, material properties and continuous description of an epithelial tissue, *Journal of The Royal Society Interface* **9**, 2614 (2012).
- [58] S. Ishihara and K. Sugimura, Bayesian inference of force dynamics during morphogenesis, *Journal of Theoretical Biology* **313**, 201–211 (2012).
- [59] N. Noll, S. J. Streichan, and B. I. Shraiman, Variational method for image-based inference of internal stress in epithelial tissues, *Physical Review X* **10**, Not available (2020).
- [60] A. G. Fletcher, M. Osterfield, R. E. Baker, and S. Y. Shvartsman, Vertex models of epithelial morphogenesis, *Biophysical Journal* **106**, 2291 (2014).
- [61] R. Farhadifar, J.-C. Röper, B. Aigouy, S. Eaton, and F. Jülicher, The influence of cell mechanics, cell-cell interactions, and proliferation on epithelial packing, *Current Biology* **17**, 2095 (2007).
- [62] A. W. Lees and S. F. Edwards, The computer study of transport processes under extreme conditions, *Journal of Physics C: Solid State Physics* **5**, 1921 (1972).
- [63] E. Bitzek, P. Koskinen, F. Gähler, M. Moseler, and P. Gumbsch, Structural relaxation made simple, *Phys. Rev. Lett.* **97**, 170201 (2006).
- [64] X. Yang, D. Bi, M. Czajkowski, M. Merkel, M. L. Manning, and M. C. Marchetti, Correlating cell shape and cellular stress in motile confluent tissues, *Proceedings of the National Academy of Sciences* (2017).
- [65] K. K. Chiou, L. Hufnagel, and B. I. Shraiman, Mechanical stress inference for two dimensional cell arrays, *PLoS Computational Biology* **8**, e1002512 (2012).
- [66] C. E. Maloney and A. Lemaître, Amorphous systems in athermal, quasistatic shear, *Phys. Rev. E* **74**, 016118 (2006).
- [67] X. Li, A. Das, and D. Bi, Mechanical heterogeneity in tissues promotes rigidity and controls cellular invasion, *Physical review letters* **123**, 058101 (2019).
- [68] N. Xu, V. Vitelli, A. J. Liu, and S. R. Nagel, Anharmonic and quasi-localized vibrations in jammed solids—modes for mechanical failure, *EPL (Europhysics Letters)* **90**, 56001 (2010).
- [69] C. Brito and M. Wyart, Heterogeneous dynamics, marginal stability and soft modes in hard sphere glasses, *Journal of Statistical Mechanics: Theory and Experiment* **2007**, L08003 (2007).
- [70] C. Maloney and A. Lemaître, Universal breakdown of elasticity at the onset of material failure, *Phys. Rev. Lett.* **93**, 195501 (2004).